Influence of spectral resolution and performance of Linear and Multilayer Perceptron models in the spectral mixture analysis

[1]João Flávio Costa dos Santos, [1]Sidney Geraldo Silveira Velloso, [2]Lais Barbosa Teodoro Alves, [1]José Marinaldo Gleriani,[2]Nilcilene das Graças Medeiros

[1]Department of Forestry. Federal University of Viçosa, ZIP code: 36570-000. Viçosa, Brazil.
[2]Department of Civil Engineering. Federal University of Viçosa, ZIP code: 36570-000. Viçosa, Brazil.

Address For Correspondence:
José Marinaldo Gleriani, Department of Forestry. Federal University of Viçosa, ZIP code: 36570-000. Viçosa, Brazil.

A R T I C L E   I N F O

A B S T R A C T

Background: The spectral mixture analysis (SMA) enables the classification of the orbital images by estimating the proportions of different features inside a mixed pixel. The great advantage of the SMA is to produce reliable results without the need for high spatial resolution images. SMA techniques have been used in the Brazilian Amazon rainforest to investigate the annual change in land cover. **Objectives:** The objectives of this paper were to evaluate the fitting of the linear spectral mixture models (LSMMs) consisting of multispectral (Advanced Land Imager) and hyperspectral (Hyperion) data, to evaluate the influence of the number of bands in the LSMM fitting, and to compare the fitting of the LSMM with a Multilayer Perceptron (MLP) model. **Results:** The Hyperion bands with the lowest correlation showed the lower values of the mean absolute error (MAE) and the use of three channels improved the fitting. The MLP model showed fewer errors than the LSMM. **Conclusion:** The results of this research indicate that the fractions images can be improved if the hyperspectral data and the MLP model are employed. Thus, the use of the Hyperion data and the MLP network is highly recommended for evaluating the deforestation in the Amazon Rainforest with SMA.

INTRODUCTION

Each type of land cover has a typical spectral response. In the orbital images, the digital numbers (DN) correspond to the average intensity of energy reflected or emitted by different targets of the surface, besides the atmospheric effects, within the instantaneous field of vision (IFOV) of the sensor (Lillesand *et al*., 2014). The picture elements (pixels) may represent a single type or multiple types of land cover spectral response. If the pixels are large, this representation is likely to refer to more than one type and feature of a mixed pixel (Lu*et al*., 2003; Tso and Mather, 2009).

The spectral mixture analysis (SMA) techniques are used to quantify the proportion of two or more components within a mixed pixel. Several techniques are involved in this approach, like linear spectral mixture models (LSMM), nonlinear spectral mixture models (NLSMM) and Multilayer Perceptron (MLP) network (Wu and Murray, 2003; Liu and Wu, 2005).

The project termed Monitoring of the Brazilian Amazon Forest by Satellite (PRODES) uses the SMA to obtain image fractions of the scene components (vegetation, soil and shadow) in order to focus information on deforestation in one or two images (Câmara *et al*., 2013). The great advantage of the SMA is to produce reliable results without the need for high spatial resolution images. PRODES, for example, utilizes the Landsat 30 m data.

As the SMA is important to the Amazonian context it is very interesting to evaluate newapproaches. We decided to investigate whether the hyperspectral data and MLP model can improve the fraction images. Predominantly, these fraction images are obtained with multispectral data and the LSMM. The objectives of this paper were to evaluate the fitting of the linear spectral mixture models (LSMMs) consisting of multispectral (Advanced Land Imager) and hyperspectral (Hyperion) data, to evaluate the influence of the number of bands in the LSMM fitting, and to compare the fitting of the LSMM with a Multilayer Perceptron (MLP) model.

MATERIALS AND METHODS

Two study areas located in the Itapuã do Oeste municipality, Rondônia, Brazil (Fig. 1) were selected for this work. Study area I comprises 23.8 km² and wasselected because it overlapsboth the Advanced Land Imagery (ALI) and the Hyperion swath widthsand because it presentsthe three components (soil, vegetation and shadow). This first area was used to study the effect of the spectral resolution on the spectral mixture model. The execution of the Multilayer Perceptron (MLP) model required data from a RapidEye image (described below). Thus, area II was defined according to the low cloud cover from the RapidEye images available. This area totaled 60.4 km².

Products of the ALI and Hyperion sensors onboard the Earth Observation (EO-1) experimental satellite were acquired on the Earth Explore website. The images are from May 27th, 2012 (path/row: 232/66).

Launched on November 21, 2000, the EO-1 was the first satellite of the New Millennium Program (NMP) under the National Aeronautics and Space Administration (NASA). This satellite mission was launched to validate and to demonstrate the NASA's new technologies for a period of one year. Next, the mission continued with the acquisition and distribution of the Hyperion hyperspectral data and ALI multispectral data, with a 16-day revisit time.
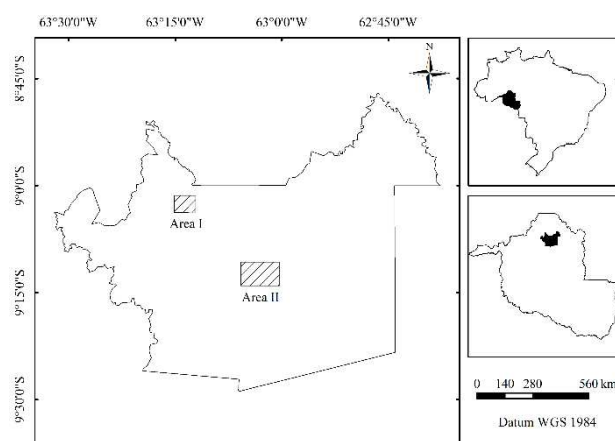

Fig. 1: Location of the two study sites (Area I and Area II) in the Itapuã do Oeste municipality,Rondônia, southwest Amazon.

The ALI sensor was designed to produce images comparable with those of the ETM+ of Landsat 7 and is considered a precursor of the OLI of Landsat 8. The ALI wavelength bands and the spatial resolution of the multispectral bands (30 m) are similar to the ETM+, barring the absence of the thermal band (band 6) and the spatial resolution of 10 m from the panchromatic band. Other novelties in this sensor include three bands 1', 4' and 5' (Table 1) and a pushbroom scanning system.The superior imaging quality of this sensor was discussed by Schowengerdt (2006). The scenes have dimensions of 37 x 185 km and product L1R (Level 1 Radiometric) images are available with 16 bits/pixel (Middleton *et al.*, 2013).

Hyperion is a 242-band hyperspectral sensor that covers the spectral range from 356 to 2577 nm, at approximately 10 nm intervals. In the L1R, 198 spectral bands radiometrically calibrated are provided (8-57 for the visible and near- infrared and 77-224 for the shortwave infrared) (Table 1). This instrument provides images with dimensions of 7.5 x 100 km and 16 bits of radiometric resolution (Goodenough et al., 2003).

Table 1: Spectral characteristics of ALI and Hyperion sensors

Δλ (nm)	BAND	Sensor Bands	
		ALI	Hyperion*
480 - 690	PAN	PAN	B-14 – B33
421 - 433		-	B8
433 - 453	MS-1'	B1	B9-B10
450 -515	MS-1	B2	B11-B16
515 - 525		-	B17
525 - 605	MS-2	B3	B18-B25
605 - 625		-	B26-B27
633 - 690	MS-3	B4	B28-B33
690 - 775		-	B34-B42
775 - 805	MS-4	B5	B43-B45
805 - 845		-	B46-B49
845 - 890	MS-4'	B6	B50-B54
890 - 1200		-	B55-B57; B77-B105
1200 - 1300	MS-5'	B7	B106-B115
1300 - 1550		-	B116-B140
1550 - 1750	MS-5	B8	B141-B-160
1750 - 2080		-	B161-B-192
2080 - 2350	MS-7	B9	B193-B-219
2350 - 2396		-	B220-B-224

* Interval of calibrated bands covering the spectral range (Δλ).

For area II, besides the ALI data, a RapidEye image (tile 2034914)acquired on August 29, 2012, was used. The RapidEye constellation includes five satellites that provide 5 m pixel sized images after resampling; five spectral bands that encompass the intervals of optical electromagnetic energy of blue (440-510 nm), green (520-590 nm), red (630-685 nm), red edge (690–730 nm) and near infrared (760-850 nm); radiometric resolution of 12 bits and daily (off-nadir) or 5.5 days (at nadir) revisit time (Tyc *et al*., 2005; RapidEye, 2011).

The original data were converted into reflectance based on equation 1. To convert the digital numbers into absolute radiance values, the following relationships were adopted: each Hyperion band of VNIR (1 to 70) and SWIR (71 to 242) was divided by its scale factor (i.e., 40 for VNIR and 80 for SWIR) (Goodenough *et al*., 2003); for ALI data, equation 2 was used and the radiometric calibration coefficients were obtained in Chander *et al*., (2009).

$$\rho_\lambda = \frac{\pi.L_\lambda.d^2}{ESUN_\lambda.\cos(\theta_s)} \tag{1}$$

where: ρ_λ – planetary TOA reflectance; L_λ – spectral radiance at the sensor's aperture [W/m^{-2}.sr^{-1}.µm^{-1}]; d – Earth-Sun distance [astronomical units]; $ESUN_\lambda$ – mean exoatmospheric solar irradiance [W/m^{-2}.µm^{-1}]; and θ_s – solar zenith angle [radians].

$$L_\lambda = \left(\frac{LMAX_\lambda - LMIN_\lambda}{Q_{calmax} - Q_{calmin}}\right)(Q_{cal} - Q_{calmin}) + LMIN_\lambda \tag{2}$$

where: L_λ – spectral radiance at the sensor's aperture [W m^{-2} sr^{-1}µm^{-1}]; $LMAX_\lambda$ – spectral at-sensor radiance scaled to Q_{calmax} [W m^{-2}sr^{-1}µm^{-1}]; $LMIN_\lambda$ – spectral at-sensor radiance scaled to Q_{calmin}[W m^{-2} sr^{-1}µm^{-1}]; Q_{calmax} – maximum quantized calibrated pixel value corresponding to $LMAX_\lambda$ [DN]; Q_{calmin} – minimum quantized calibrated pixel value corresponding to $LMIN_\lambda$[DN]; and Q_{cal} – quantized calibrated pixel value [DN].

Linear Spectral Mixture Model (LSMM):

TheLSMM assumes that the response expressed in a pixel is an additive function of the spectral response expressed by each individual feature, proportionally weighted by the area it occupies in the pixel (Tso and Mather, 2009).

The LSMM was processed in the SPRING 5.3 *software* system (Câmara *et al*., 1996). It was necessary to change the file of the spectral_bands to implement the spectral information of the ALI and Hyperion sensors. The fraction images (mix) of the LSMM are processed in SPRING with 8 bits and integer numbers. Therefore, due to compatibility issues, the reflectance of the float grid was multiplied by 255 in order to produce an integer grid.

The LSMM is based on the premise that the spectral response of each pixel in any wavelength can be considered as the linear sum of the spectra of the endmembers (Powell *et al*., 2007). The model (equation 3) is able to separate the constituents of each pixel of the scene proportionally and to generate the fraction images (Quintano *et al*., 2013). Thus:

$$\rho_i = \sum_{j=1}^{n}(a_{ij}x_j) + e_i \tag{3}$$

where: ρ_i – spectral reflectance of a pixel in the i^{-th} band; *n*- the number of endmembers; a_{ij} – spectral reflectance of j^{-th} endmember on i^{-th} spectral band; x_j – theproportion of the component within the j-th pixel; and e$_i$ -error associated with the i-th spectral band.

If the number of the endmembers is equal or lower than the number of spectral bands, the system of linear equations derived from equation 3 is determined and the LSMM may be solved by the least squares method (Shimabukuro and Smith, 1991). This approach aims at reducing the errors in the separation of the pixel fractions.

Two restrictions are included in this model: (I) the sum of the component proportions of the pixel must be equal to 1.0 and, (II) the proportions of the pixels must range between 0 and 1.0 to have physical meaning. In SPRING, the use of the latest restriction is optional. When this restriction is implemented, the pixel value in the fraction image is obtained by multiplying the proportions (between zero and one) by 255. If this restriction is not utilized, the proportion values are scaled to the range of 100 to 200 and the pixels with the negative values or values greater than one appear outside this range. In the latter case, the number of pixels outside the range of physical meaning, observed in the image histograms, indicates inadequate models or a poor definition of pure pixels (Tso and Mather, 2009; INPE, 2015). Thus, this type of analysis also facilitates the assessment of the adequacy of the mixture model (Anderson *et al*., 2005).

Two scenarios were used in this paper: the adoption and non-adoption of the restriction II. Without adopting restriction II, the pixels out of the range of physical meaning were quantified. When the restriction was adopted, the mean absolute error (MAE) (Van de Voorde, 2009) was calculated according to equation 4:

$$MAE_i = \frac{\sum_{k=1}^{M}\left|\rho_i - \left(\sum_{j=1}^{n} a_{ij} x_j\right)\right|}{M} \tag{4}$$

where: MAE – mean absolute error of i[-th] spectral band; M – number of pixels in the scene; ρ_i – spectral reflectance of a pixel in the i[-th] band; n – number of endmembers; a_{ij}– spectral reflectance of j[-th] endmember on i[-th] spectral band; x_j – proportion of the component within the j[-th] pixel.

Endmember selection to LSMM:

The endmember is a pure pixel (or the purest pixel found in the image) which is expected to contain only one component (vegetation, soil or shadow, in the present work). One approach to define the pure components is the selection of representative pixels in the images themselves, through the scatterplots between the spectral bands (Wu and Murray, 2003; Dawelbait and Morari, 2012). One advantage of this technique is that the endmembers are selected based on the spectral variability inherent to an image data, without the need of a pixel totally pure.

In this study, according to Dawelbait and Morari (2012), the Principal Component Analysis technique is used to reduce data dimensionality. The first two components were selected to constitute the axes of the scatterplot because they include the largest number of uncorrelated information. Three endmembers (soil, shadow and vegetation) were selected in the two study areas for the LSMM

Selection of bands to compose models:

Generally, all the bands of an orbital sensor are used to compose the LSMM. However, the quality of the models are evaluated with different numbers of bands for the ALI sensor. The first two bands of this sensor were not included in the model because we did not performthe atmospheric correction step and these bands are the most affected by atmospheric scattering. The Hyperion bands, which correspond to the mentioned ALI bands, presented noise. This noise highlights the stripping effect that is caused by the incoherent calibration of the detectors of the sensor(Goodenough *et al*., 2003).

After analyzing the results of the LSMM for the ALI sensor, the Hyperion bands related to the central wavelengths of the ALI bands were chosen for comparison purposes.

In most cases, the best design is compounded by the less correlated bands (Theseira *et al*., 2002). Thus, a correlation table between the ALI bands facilitated the selection of the bands for the models. The best LSMM model for the ALI sensor in area I was also performed in area II and served as a comparative criterion for the MLP model.

Multilayer Perceptron Model:

One MLP model was structured in the SNNS software system (Stuttgart Neural Network Simulator) (Zell *et al*., 1998). Liu and Wu (2005) highlight MLP as the most accurate nonlinear model. The network was structured with three input neurons (referring to ALI bands 3, 4, and 5 (see results)), 9 neurons in the hidden layer, and three output neurons (referring to the proportion of soil, vegetation and shadow) (Fig.2). Sigmoid logistics was the activation function used.
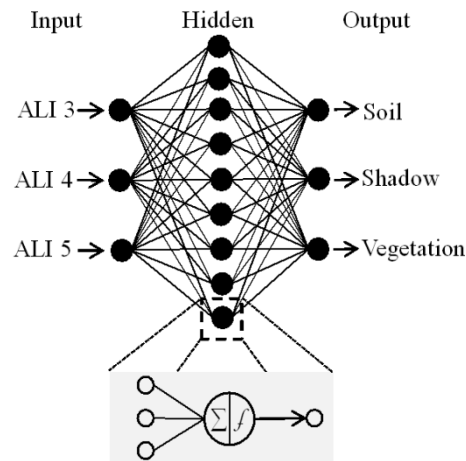
Fig.2: Structure of the Multilayer Perceptron (MLP) network to obtain the fraction images (soil, shadow and vegetation) from the bands 3, 4 and 5 of the Advanced Land Imager sensor (ALI).

For model training purposes, 300 cycles were used along with the error backpropagation algorithm and a learning rate (η) of 0.1. Pixels (5 m) from the thematic classification of the RapidEye image were adopted as the reference to the output data. Each pixel of the ALI sensor (900m²) is spatially equivalent to the dimension of 36 pixels from a RapidEye image. Therefore, a zonal count was executed in a vector grid coincident with the ALI pixels to determine the proportion of each class (soil, shadow and vegetation) in the ALI pixels sampled. The supervised classification of the RapidEye image was processed with the maximum likelihood (MAXVER), pixel-by-pixel, algorithm. The training procedure was performed with approximately 10% of the total area. A similar methodology was adopted by Foody *et al.* (1997), Liu and Wu (2005) and Van De Voorde *et al.* (2009)*.*

To evaluate the performance of the MLP and LSMM models in area II, the MAEs were calculated by the difference between the fraction images generated from each model and the reference fraction images obtained from the RapidEye thematic map (reference data).

Results:

For area I, the first two principal components (PC) were used to display the scatterplot (Figure 3), representing 96.45% of the variance between the image bands of the sensor ALI, and 94.32% of the variance between the image bands of the Hyperion. The scatterplot of the first two PCs for the ALI sensor (Fig.3-A) defined the image of a triangle better than that given by the Hyperion sensor (Fig.3-B).
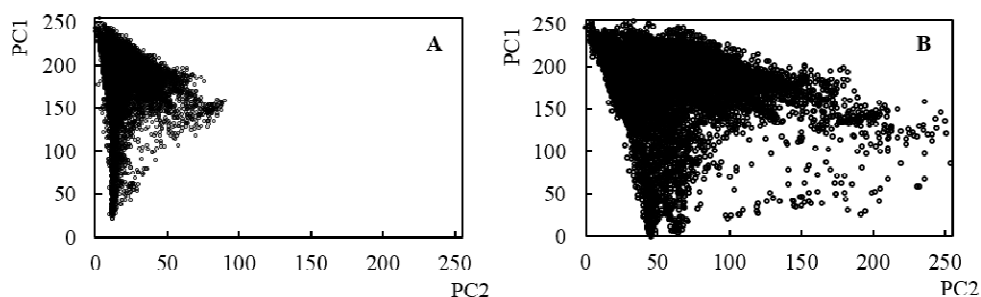

Fig. 3: Scatterplot between the first and second principal components (PCs) from the ALI (A) and Hyperion (B) image sensors.

The endmembers were selected in the scatterplot (the most extreme point on each side of the imaginary triangle formed by the distribution of the pixels values). They enabled the representation of the spectral response in the ALI bands (Fig.4-A) and in the corresponding Hyperion bands (related to the central wavelengths of the ALI bands) (Fig. 4-B). Both the multispectral (larger wavelength interval ($\Delta\lambda$)) and hyperspectral (smaller wavelength interval ($\Delta\lambda$)) data indicated the endmembers of the vegetation, soil and shadow in the same locations.
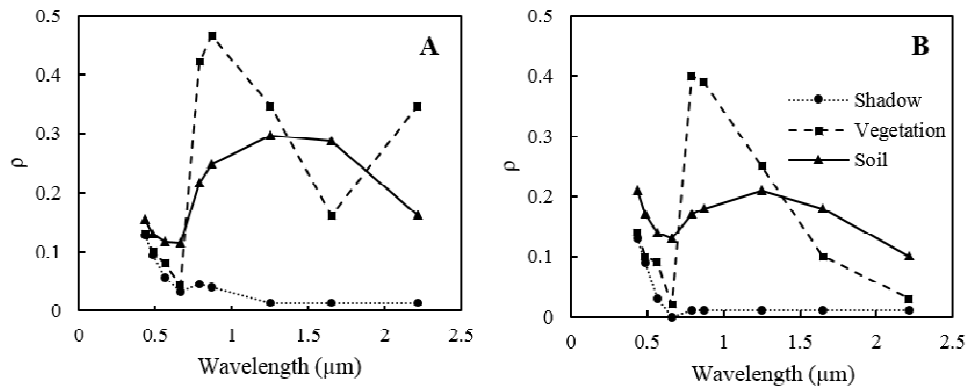
Fig.4: Spectral response (ρ) of endmembers in multispectral bands image ALI (A) and central bands (corresponding to ALI bands) of hyperspectral sensor Hyperion (B).

Next, the LSMM was structured with different compositions and number of bands of the ALI and Hyperion sensors. To compose the models with three bands, those less correlated were preferred. The models with the less correlated bands were formed by bands 3, 4 and 4' for the ALI sensor (Table 2) and by bands 31, 44 and 55 for the Hyperion sensor (Table 3).

Table 2: Correlation matrix between ALI bands

Bands	2	3	4	4'	5'	5	7
2	1	0.917	0.442	0.403	0.523	0.841	0.851
3		1	0.168	0.140	0.337	0.808	0.912
4			1	0.993	0.919	0.590	0.333
4'				1	0.935	0.582	0.319
5'					1	0.774	0.545
5						1	0.945
7							1

Table 3: Correlation matrix between Hyperion bands with central wavelengths to the ALI sensor

Bands	21	31	44	51	111	151	206
21	1	0.937	0.602	0.554	0.566	0.863	0.881
31		1	0.368	0.323	0.405	0.836	0.911
44			1	0.995	0.899	0.660	0.497
51				1	0.915	0.641	0.466
111					1	0.783	0.593
151						1	0.935
206							1

On analyzing the values of the MAE and the percentage of inconsistent values (Table 4), it was perceived that the models formed by the three less correlated bands showed good results. Besides, the models with the fewer number of bands showed the higher performance. Thus, it is logical to conclude that the models of best performance produced the best fraction images (Fig.5).

Table 4: Performance of linear models tested for multispectral ALI sensor and hyperspectral Hyperion sensor

	Sensor	ALI Band	2	3	4	4'	5'	5	7	Inconsistent Values (%)
Absolute		2/3/4/4'/5'/5/67	2.42	3.85	7.31	8.64	28.2	25.7	4.95	6.7
		3/4/4'/5'/5	_	4.85	8.64	9.93	25.54	26.72	_	4.57
		3/4/4'/5'	_	3.29	1.49	1.34	2.89	_	_	3.63
Mean Error	ALI	3/4/5	_	1.68	0.95	_	_	1.52	_	2.44
		3/4/4'	_	2.05	2.13	1.65	_	_	_	14.45

			21	31	44	51	111	151	206	
		Model 3/4'/5	_	1.67	_	1.51	1.45	_	_	2.42
	Sensor	Hyperion Band	21	31	44	51	111	151	206	
Mean Absolute Error	Hyperion	21/31/44/51/111/151/206	12.53	17.47	19.83	13.24	28.38	5.01	9.45	8.48
		31/44/51/111/151	_	6.85	12.50	18.18	23.12	7.47	_	2.02
		31/44/51/111	_	3.71	9.16	2.47	4.83	_	_	1.31
		31/44/151	_	6.17	1.04	_	_	2.37	_	1.61
		31/44/51	_	1.84	0.75	1.25	_	_	_	0.85
		31/51/111	_	3.73	_	3.14	5.27	_	_	1.66
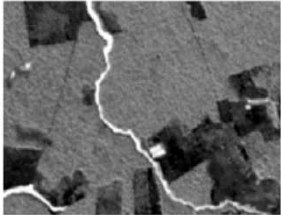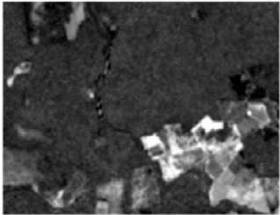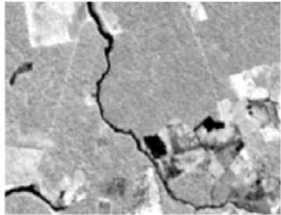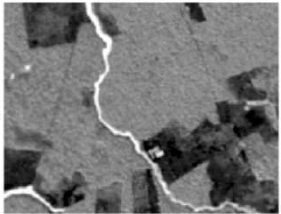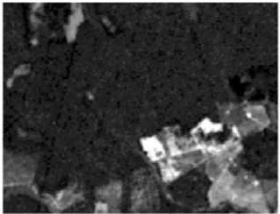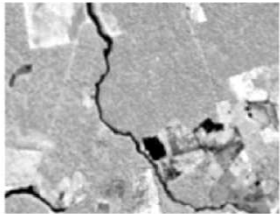
Fig. 5: Fractions images of soil, shadow and vegetation generated by the linear spectral mixture models that presented the best fitting for multispectral (ALI) and hyperspectral (Hyperion) data. Brighter areas indicate higher proportion of the components in these monochromatic fraction images.

The performance of the MLP model in area II was assessed employing the best results obtained from the ALI data for area I (the model with three bands, 3, 4 and 5 (Table 4)) as comparative data. A register, screen-by-screen, between RapidEye and the ALI images was performed, with the selection of 21 control points and the use of a 3rd degree polynomial. After geometric correction, a root mean square error (RMSE) value less than 0.5 was computed. The fractions images generated by the LSMM and MLP models were compared with the reference data which were obtained by the supervised classification of the RapidEye image (Fig.6). The results of this comparison indicated that the MLP presented fewer MAE values than the LSMM (Table 5).
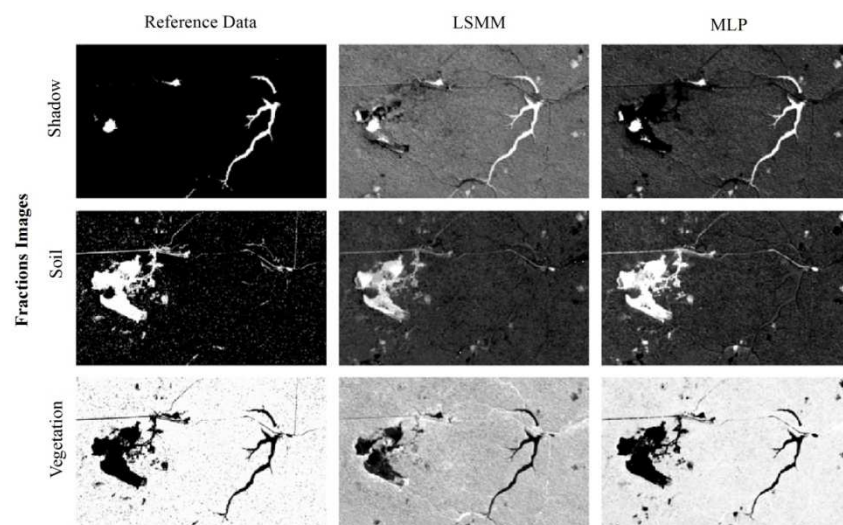

Fig.6: Fractions images of soil, shadow and vegetation generated by the supervised classification of the RapidEye image (reference data), linear spectral mixture model (LSMM) and multilayer perceptron

(MLP) model. The reference data was used to calculate the Mean Absolute Error (MAE) to area II. Brighter areas indicate higher proportion of the components in these monochromatic fraction images.

Table 5: Mean Absolute Error in the multilayer perceptron (MLP) and linear spectral mixture model (LSMM)

	MLP	LSMM
Shadow	0.1213	0.5037
Soil	0.0874	0.3748
Vegetation	0.0966	0.3431

Discussion:

The principal components analysis (PCA) technique helped to reduce spectral redundancy for both sensors given that the first two principal components (PCs) explained more than 94% of the total variance. These PCs also facilitated the selection of the endmembers in the scene. The low correlation existing between them facilitated visualization of the geometry of a triangle when the dispersion of the digital numbers (Figure 3) was plotted. The endmembers were selected by identifying the vertices of the triangle formed.

The key in achievingsuccess in the LSMM is to accurate select the endmembers (Elmore*et al*., 2000; Dawelbait and Morari, 2012). Theoretically, if all the pixels inside the triangle are defined by the endmembers, the mixture model can be considered to be an ideal linear model (Wu and Murray, 2003). Thus, for area I, the linear model can be used to describe the spectral mixture (Fig.3-A). However, the noise level in the Hyperion bands, also identified by Goodenough *et al*. (2003), made it difficult to define the geometry of a triangle (Fig.3-B).

The comparison between the models of the ALI sensor and those formed by the corresponding Hyperion bands showed that the percentage of values outside the physical meaning range (i.e. $0 \leq X \leq 1$) is expected to be higher in the latter. Goodenough *et al*. (2003) described some procedures that helped to remove the noise from the Hyperion images, although they were not used in this work.

The models that included more bands produced higher values for theMAE and the highest percentage of inconsistent values (Table 4). This behavior may be related to the correlation among the bands. When the number of bands is large, the LSMM must be carefully applied, as some bands are highly correlated (Tso and Mather, 2009) (Tables 2 and 3).

The bands 3, 4 and 4', from the ALI sensor, showed the least correlation (Table 2). However, the performance of the model that considered these three bands was inferior to that which employed bands 3, 4, and 5 (Table 4). For the Hyperion data, it was evident that the less correlated bands (31, 44, 51) (Table 3) formed the model with the lowest MAE values per band and lowest percentage of inconsistent values (Table 4).

The spectral behavior of the endmembers for area I (Fig.4) shows certain deviations from the curves commonly recorded in the literature (Tso and Mather, 2009; Lillesand*et al*., 2014). This result indicates that the reference pixels selected in this area are not totally pure. In practice, it is difficult to find in nature a square area of 900 m² exclusively composed of soil or vegetation or completely shaded. Thus, the selection of the endmember in the image itself eliminated the need for completely pure pixels as a reference, which is one major advantage of this methodology. Besides, the atmospheric scattering and absorption effects are included in this spectral response. The Amazon basin is greatly influenced by atmospheric effects which affect the spectral behavior (Lu *et al*.,2002).

The spectral response (ρ) of the endmember components of vegetation was found in an area of regrowth. This result facilitates the understanding that in areas of native forest, canopy stratification caused an intense presence of shadows, which prevented the detection of a pure pixel of vegetation in those areas (Shimabukuro *et al*., 1998). The soil response was expressed in regions having bare soil and the shadow response was expressed in locations with water bodies. The observation of the fraction images of soil, shadow and vegetation (Fig.5) indicates that some portion of vegetation prevails in the scene, followed by portions of shadow and soil, in this sequence.

Despite the good performance of the hyperspectral data from Hyperion, the scarcity of the data available and relatively narrow coverage range are aspects causing concern. Multispectral images, including the Landsat series, cover almost the whole globe and can be easily accessed. This enabled a comparison between the performance of the MLP and the LSMM.

The results of the present work indicated a better MLP performance when compared with the LSMM (Table 5). These results agree with those reported by many authors in the literature (Foody *et al*. 1997; Carpenter *et al*., 1999; Liu and Wu, 2005; Van De Voorde *et al*., 2009). Besides, Liu and Wu (2005) reported better performance with the MLP when compared to the ARTMAP network.

One way to apply the MLP model is to use high spatial resolution data from a small fraction of the territory for network training and generalize it to the whole area covered by the lower resolution image (Liu and Wu, 2005; Van de Voorde *et al*., 2009). This application is very interesting for large areas such as the ones covered by PRODES. Thus, this method reveals the advantage of reducing the cost of acquiring high-resolution images and requires less processing power and data storage.

One of the steps of assessing deforestation in the Amazon Rainforest is the application of spectral mixture analysis techniques to obtain fraction images to identify areas without shadows (areas of bare soil or regrowth) (Câmara *et al*., 2013). Thus, the results of this study can provide crucial information for ensuring accurate applications of the mixture models.

Conclusions:

The results demonstrate that the LSMMs formed by three bands (especially the regions of green, red and near infrared) present a lower value for MAE when compared with the models having a higher number of bands. Hyperspectral data from Hyperion, especially bands 31, 44 and 51, increased the accuracy of the linear mixture models. The linear model, however, was not as accurate as the MLP. Thus, for evaluating the deforestation in the Amazon Rainforest with mixture analysis, the use of the MLP network is highly recommended.

ACKNOWLEDGMENTS

REFERENCES

Anderson, L.O.,L.E.Oliveira, C.Aragão, A.Lima and Y.E. Shimabukuro, 2005. Detecção de cicatrizes de áreas queimadas baseada no modelo linear de mistura espectral e imagens índice de vegetação utilizando dados multitemporais do sensor MODIS/TERRA no estado do Mato Grosso, Amazônia brasileira. Acta Amazonica, 35(4): 445-456.

Câmara, G.,R.C.M.Souza, U.M.Freitas andJ. Garrido, 1996. SPRING: Integrating remote sensing and GIS by object-oriented data modelling. Computers & Graphics, 20(3): 395-403.

Câmara, G.,D.M.Valeriano andV.S. Soares, 2013. Metodologia para o Cálculo da Taxa Anual de Desmatamento na Amazônia Legal. Instituto Nacional de Pesquisas Espaciais – INPE, São José dos Campos, São Paulo. 24p. (http://www.obt.inpe.br/prodes/metodologia_TaxaProdes.pdf). Accessed on 01/11/2015.

Carpenter, G.A.,S.Gopal, S.Macomber, S.Martens andC.E. Woodcock, 1999. A neural network method for mixture estimation for vegetation mapping. Remote Sensing of Environment, 70(2): 138-152.

Chander, G.,B.L.Markham andD.L. Helder, 2009. Summary of current radiometric calibration coefficients for Landsat MSS, TM, ETM+, and EO-1 ALI sensors. Remote Sensing of Environment, 113(5): 893-903.

Dawelbait, M. and F. Morari, 2012. Monitoring desertification in a Savannah region in Sudan using Landsat images and spectral mixture analysis. Journal of Arid Environ, 80: 45-55.

Elmore, A.J.,J.F.Mustard, S.J.Manning and D.B. Lobell, 2000. Quantifying Vegetation Change in Semiarid Environments. Remote Sensing of Environment, 73(1): 87-102.

Foody, G.M.,R.M.Lucas, P.J.Curran andM. Honzak, 1997. Non-linear mixture modeling without end-members using an artificial neural network. International Journal of Remote Sensing, 18(4): 937-953.

Goodenough, D.G.,A.Dyk, K.O.Niemann, J.S.Pearlman, S.Member,H.Chen, T.Han,M.Murdoch andC. West, 2003. Processing Hyperion and ALI for Forest Classification. IEEE Transactions on Geoscience and Remote Sensing, 41(6): 1321-1331.

INPE, 2015. Tutorial de geoprocessamento, modelos de mistura (http://www.dpi.inpe.br/spring/portugues/tutorial/modelos.html). Acessed on 01/11/2015.

Lillesand, T.,R.W.Kiefer andJ. Chipman, 2014. Remote sensing and image interpretation. 7th ed. John Wiley & Sons, New York, pp: 763.

Liu, W. andE.Y. Wu, 2005. Comparison of non-linear mixture models: sub-pixel classification. Remote Sensing of Environment, 94(2): 145-154.

Lu, D.,P.Mausel, E.Brondizio andE. Moran, 2002. Assessment to atmospheric correction methods for Landsat TM data applicable to Amazon basin LBA research. International Journal of Remote Sensing, 23(13): 2651-2671.

Lu, D.,E.Moran andM. Batistella, 2003. Linear mixture model applied to Amazonian vegetation classification. Remote Sensing of Environment, 87(4): 456-469.

Middleton, E.M.,S.G.Ungar, D.J.Mandl, L.Ong, S.W.Frye, P.E.Campbell, D.R.Landis, J.P.Young andN.H. Pollack, 2013. The earth observing one (EO-1) satellite mission: Over a decade in space. IEEE Journal of Selected Topics in Applied Earth Observations and Remote Sensing, 6(2): 243-256.

Powell, R.L.,D.A.Roberts, P.E.Dennison andL.L. Hess, 2007. Sub-pixel mapping of urban land cover using multiple endmember spectral mixture analysis: Manaus, Brazil. Remote Sensing of Environment, 106(2): 253-267.

Quintano, C.,A. Fernández-Manso andD.A. Roberts, 2013. Multiple Endmember Spectral Mixture Analysis (MESMA) to map burn severity levels from Landsat images in Mediterranean countries. Remote Sensing of

Environment, 136: 76-88.

RapidEye, A.G., 2011. Satellite imagery product specifications. (http://www2.flyby.it). Accessed on 13/05/2016.

Schowengerdt, R.A., 2006. Remote sensing: models and methods for image processing. 3nd ed. Academic press, Arizona, p: 515.

Shimabukuro, Y.E.,G.T.Batista, E.M.K.Mello, J.C.Moreira and V. Duarte, 1998. Using a shade fraction image segmentation to evaluate desforestation in Landsat Thematic Mapper images of the Amazon Region. International Journal of Remote Sensing, 19(13):535-541.

Shimabukuro, Y.E. and J.A.Smith, 1991. The least-squares mixing models to generate fraction images derived from remote sensing multispectral data. IEEE Transactions on Geoscience and Remote Sensing, 299(1): 16-20.

Theseira, M.A.,G.Thomas and C.A.D. Sannier, 2002. An evaluation of spectral mixture modelling applied to a semi-arid environment. International Journal of Remote Sensing, 23(4): 37-41.

Tso, B. andP. Mather, 2009. Classification methods for remotely sensed data. 2nd ed. Taylor & Francis, New York, p: 356.

Tyc, G.,J.Tulip, D.Schulten, M.Krischke and M. Oxfort, 2005. The RapidEye mission design. Acta Astronautica, 56(1): 213-219.

Van de Voorde, T.,T.Roeck andF. Canters, 2009. A comparison of two spectral mixture modeling approaches for impervious surface mapping in urban areas. International Journal of Remote Sensing, 30(18): 4785-4806.

Wu, C. and A.T. Murray, 2003. Estimating impervious surface distribution by spectral mixture analysis. Remote Sensing of Environment, 84(4): 493-505.

Zell, A.,G.Mamier, M.V.N.Mache, R.Hübner,S.Dörin, K-U. Hermann *et al*., 1998. SNNS – Stuttgart Neural Network Simulator v.4.2, User Manual. University of Stuttgart/ University of Tübingen, Germany, p: 338.